Journal of Power Sources 450 (2020) 227593

Contents lists available at ScienceDirect

Journal of Power Sources

journal homepage: www.elsevier.com/locate/jpowsour

Tailoring the interfaces of silicon/carbon nanotube for high rate lithium-ion battery anodes

Ziqi Zhang [a], Xiang Han [a], Lianchuan Li [a], Pengfei Su [a], Wei Huang [a], Jianyuan Wang [a], Jianfang Xu [a], Cheng Li [a], Songyan Chen [a,*], Yong Yang [b,**]

[a] Department of Physics, Jiujiang Research Institute and Collaborative Innovation Center for Optoelectronic Semiconductors and Efficient Devices, Xiamen University, Fujian, 361005, People's Republic of China

[b] State Key Laboratory for Physical Chemistry of Solid Surfaces, Department of Chemistry, Xiamen University, Fujian, 361005, People's Republic of China

HIGHLIGHTS

- Inactive Cu_3Si patches act as joints between silicon powders and carbon nanotubes.
- Carbon nanotubes supply a self-adapted and high-efficiency electronic network.
- The conductive network is still active despite mechanical fracture of electrodes.
- Simple synthesis and low cost make it possible for industrial employments.

ARTICLE INFO

Keywords:
Micrometer-sized silicon anodes
Carbon nanotubes
Cu_3Si silicide
High rate
Structural stability

ABSTRACT

Micrometer-sized silicon powders, due to its high specific capacity, easy accessibility, and low cost, have been regarded as an attractive anode material for lithium-ion batteries. The severer mechanical instability and high inter-particle resistance during cycling, however, hinder its further application. In this work, a novel potholed micrometer-sized silicon powders (PMSi)/carbon nanotubes (CNT)/C electrode is proposed. The resulting three-dimensional (3D) conductive framework and multi-point contact network exhibit ideal structural stability and high-rate cycling property. Hence, the volume resistivity of PMSi/CNT/C (157 Ω m) is reduced significantly relative to traditional PMSi/commercial carbon nanotubes (CCT)/C composite (400 Ω m). By testing the fabricated half-cell LIB with the PMSi/CNT/C composite anode, high reversible specific capacity of 2533 mAh g^{-1} with a remarkable high initial coulombic efficiency of 89.07% and over 840 mA h g^{-1} for 1000 cycles at 2 A g^{-1} is measured. Even at the rate of 20 A g^{-1}, the PMSi/CNT/C electrode shows a capacity of 463 mAh g^{-1}. A full cell contained the PMSi/CNT/C anode and a $LiFePO_4/LiMn_2O_4$ cathode successfully ignites an LED array (~1.5 W), further demonstrating its outstanding electrical driving property.

1. Introduction

Increasing the energy density of lithium-ion batteries has always been a hot research spot to meet the growing demands for digital terminals, electrical vehicles, and energy-storage facilities. Currently the anode materials for commercial lithium-ion batteries are mostly based on carbon which is encountering its bottlenecks in specific capacity, e.g. graphite (372 mAh g^{-1}). Various alternative anode materials, such as silicon, metallic oxides, and lithium metal have been proposed, among which silicon is regarded as one of the most promising materials owning to its highest theoretical capacity (4200 mAh g^{-1}) and low discharge potential (0.4 V) [1–3]. However, the huge volume expansion (~300%) of silicon during charge results in mechanical fracture, loss of inter-particle electrical contact, and repeated chemical side reactions with the electrolyte [4–8]. Silicon nanostructures are widely studied and believed to sustain large volume change without mechanical fracture due to the small size and the available surrounding void space. To date, plenty of impressive works based on nano-silicon anodes have been reported and outstanding electrochemical performance is obtained [9–15]. As for micrometer-sized silicon (MSi), high compact density, less

* Corresponding author.
** Corresponding author.
E-mail address: sychen@xmu.edu.cn (S. Chen).

https://doi.org/10.1016/j.jpowsour.2019.227593
Received 9 September 2019; Received in revised form 18 November 2019; Accepted 8 December 2019
Available online 18 December 2019
0378-7753/

Interfacial side reaction low cost and easy accessibility from industrial waste makes it more attractive for industrial application. Nevertheless, MSi exhibits a weaker performance than nano-silicon anode both in cycle performance and rate capability. Sever pulverization of the MSi and high resistances between micrometer-sized silicon particles in electrode reaction process lowered the capacity and restrain the rate capability [16,17].

Two challenges remain to overcome for MSi anode, 1) Huge bulk resistance and contact resistance of MSi cause the large polarization effect and weak rate capability. An elaborate design of effective and efficient electrical network in MSi anode is necessary. 2) Severer pulverization of the MSi will lead to the invalid contact with current collector and electrochemical inactivation. A robust or self-adapted constraint is required to improve the MSi anode structure. Normally, as an additive material, carbon nanotubes (CNTs) possess excellent mechanical strength and high conductivity due to its special structure of sp [2] hybridization and half-filled π band for carbon atoms [18]. Though adding CNTs into the MSi electrode is demonstrated to enhance the total electrical conductivity [19–22], however, the physical mixing process of CNTs with MSi leads to serious agglomeration, nonuniform distribution and easy detachment. That is to say, traditional mixing method fails to take full advantages of CNTs' excellent properties.

Herein, a novel electrode structure potholed micrometer-sized silicon powders (PMSi)/CNT/C is fabricated and analyzed. 1) To significantly reduce the huge bulk resistance and contact resistance of MSi, a CNT electrical network is introduced. One end of CNT takes root in the PMSi, while the other end is curved and wound around PMSi evenly and tightly. The CNTs supply a self-adapted and multi-point contact electronic network to resist the severe volume changes during cycling. The one-end-contact mode between CNTs and PMSi makes it easy that electron transport along the CNT axis, exerting its ability to conduct electricity at the greatest extent. 2) To increase the content and uniformity of carbon nanotubes, high density tiny potholes are etched on the smooth surface of the micrometer-sized silicon powders. 3) To improve the mechanical adhesion for CNTs on Si, copper nanoparticles are adopted to catalyze the growth of CNTs. Cu_3Si patch, which formed in the following processes, is conductive and chemically inert, so that it ensures the stability of the contact point. Even if mechanical fracture of PMSi occurs in the subsequent battery cycle process, CNTs will not detach from the silicon particles (Fig. 1). 4) To establish a stable interface, a carbon shell is adopted to shield the entire particle. The carbon shell provides not only a three-dimensional conductive framework but also a stable solid electrolyte interface (SEI). As a result, the volume resistivity of PMSi/CNT/C is reduced significantly relative to traditional PMSi/commercial carbon nanotubes (CCT)/C composite. By testing the fabricated half-cell LIB using PMSi/CNT/C structured anode, high reversible specific capacity of 2533 mAh g^{-1} with a remarkable high initial coulombic efficiency of 89.07% and over 840 mA h g^{-1} for 1000 cycles at 2 A g^{-1} was measured. Even at the rate of 20 A g^{-1}, the PMSi/CNT/C electrode showed a capacity of 463 mAh g^{-1}, which is larger than the theoretical capacity of graphite. The full cell contained the PMSi/CNT/C anode and a $LiFePO_4/LiMn_2O_4$ cathode successfully ignited an LED array (~1.5 W), further demonstrates its outstanding electrical driving property.

2. Results and discussion

Fig. 2a shows the synthesis process of PMSi/CNT/C. Low-cost photovoltaic industry cutting scrap polysilicon powder (1–3 μm) is introduced as a raw material. After porosity process, the pinecone-like polysilicon particles were adopted as substrates to vertically grow CNTs induced by copper particles and then shielded by a carbon shell to form PMSi/CNT/C composite. The corresponding morphology evolution of the PMSi/CNT/C material during the synthesizing is shown in Fig. 2b–f by SEM. Smooth surface of the micrometer-sized silicon powders (Fig. 2b) become potholed after copper-assisted etching. The potholes, which distributed uniformly over the surfaces with diameters, ranging from 10 nm to 30 nm, are pitfalls to trap copper catalyst nanoparticles (Fig. 2c). A high specific surface area is not what we wanted, as it does not favor for high initial coulomb efficiency or a stable interface. The Brunauer–Emmett–Teller (BET) surface area of the MSi, PMSi, and nano silicon powders (30 nm in averaging diameter) were measured for comparison as 5 m^2 g^{-1}, 8 m^2 g^{-1}, and 52.3 m^2 g^{-1} respectively. The specific surface area of the PMSi is slightly higher than MSi, but still far less than that of nanometer silicon powders. Copper nanoparticles with similar scale of the potholes were dispersed and anchored in the potholes of PMSi by liquid phase method (Fig. 2d). It was also confirmed through energy-dispersive X-ray spectroscopy (EDS) analysis that Cu (yellow) elements are extremely well distributed in the PMSi (blue) secondary structure (Fig. 2g). From the SEM images in Fig. 2e and TEM images in Fig. 2h, since defects exist and moderate amounts five-round carbon rings or seven-round carbon rings are

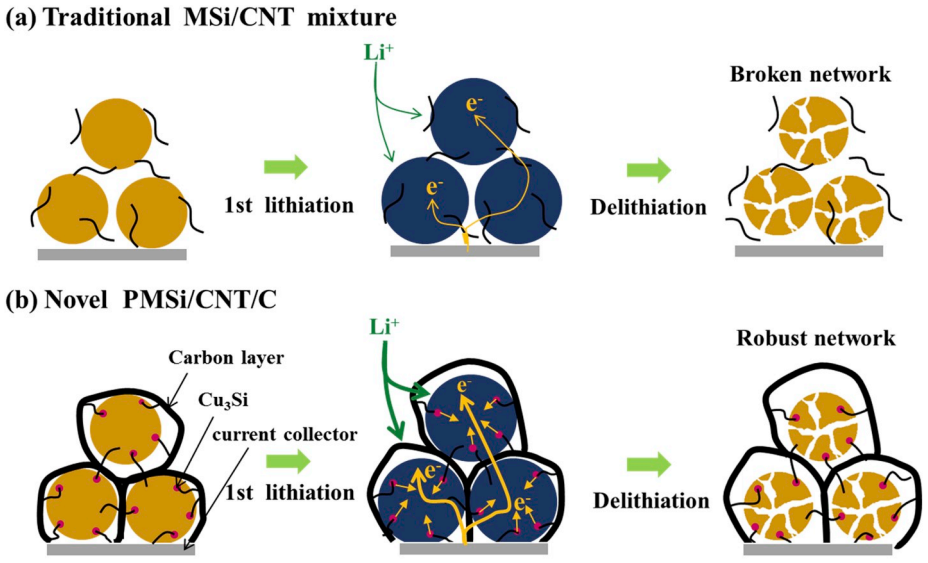

Fig. 1. Schematic comparison of the lithiation/delithiation processes in two electrode structures, (a) the traditional MSi/CNT shows broken electrical network, and (b) the novel MSi/CNT/C exhibits robust electrical network, enabled by the CNTs with one end rooted in MSi through Cu_3Si silicide while the other end embedded in carbon layer.

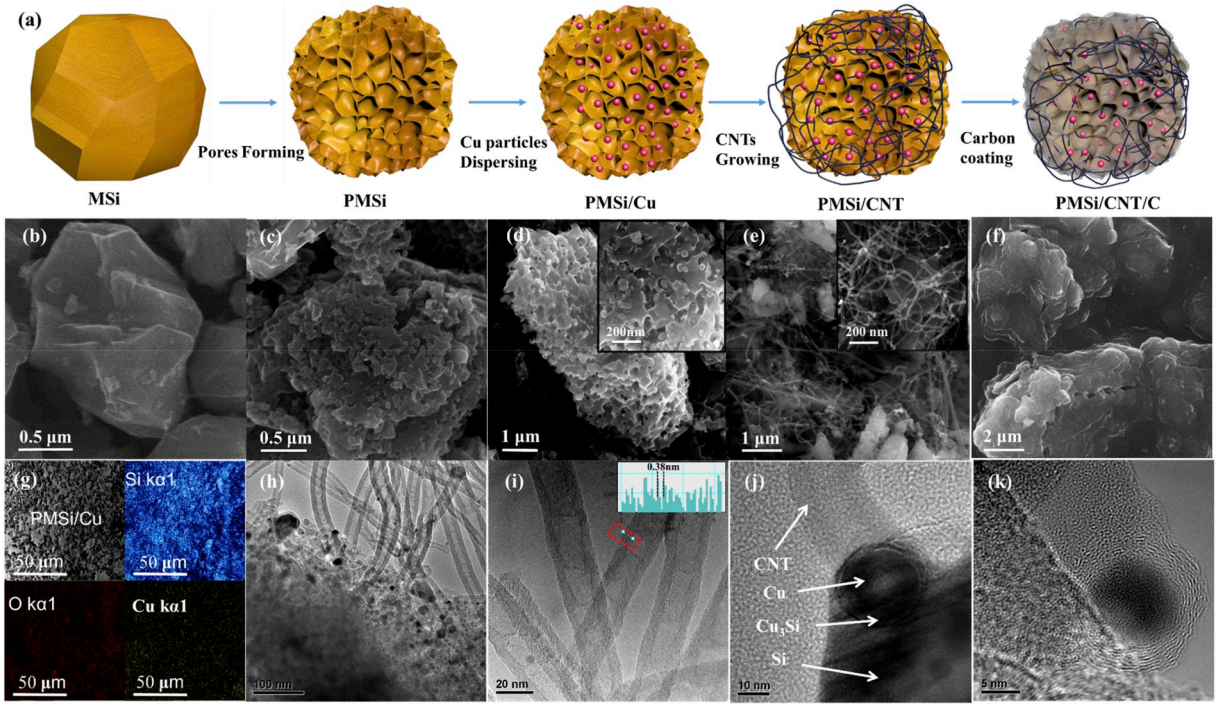

Fig. 2. (a) The schematic synthetic process of PMSi/CNT/C. SEM images of the MSi (b), the PMSi (c), the PMSi/Cu (d), the PMSi/CNT (e), and the PMSi/CNT/C composite electrode (f). (g) EDS elemental mapping of PMSi/Cu. TEM images of the PMSi/CNT/C (h), the CNTs(i), a typical CNT grown from a copper particle (j) and the contact mode between CNTs and PMSi.

introduced in the structure, CNTs are curved and wound around PMSi particles evenly and tightly [23,24], with one end stuck tightly to the surface of PMSi. No agglomeration of CNTs was found. The pipe diameters, ranging from 10 nm to 30 nm, are consistent with the size of the potholes and Cu particles on PMSi. The contents of C, H, and N for PMSi/CNT were 0.7 wt%, 0.2 wt%, and 0.2 wt% respectively as estimated by elemental analysis. The low carbon content indicates that the weight percentage of the CNTs in the PMSi/CNT composite is very tiny and negligible when evaluating the composite's total battery capacity. To further improve the conductivity and provide a passivation layer for the PMSi/CNT, a carbon layer generated from polyacrylonitrile (PAN) during carbonization process was coated onto the material's surface (Fig. 2f). This carbon layer is substantially uniformly coated on PMSi/CNT particles except some sharp edges and corners, and the electrode is relatively smooth (Fig. S1 a-b). From elemental mapping, carbon is evenly distributed in accord with silicon (Fig. S1 c-f). It can act as an artificial SEI and binder to improve the cycle stability of the electrodes, which has been confirmed in our previous works [25–28]. After carbon layer wrapping, contents of C, H, and N were increased to 18.3%, 0.7%, and 3.9%, respectively. The other 77.1% was silicon.

Detailed structure TEM image in Fig. 2i demonstrates that the CNTs consist of ~15 coaxial cannulas with a interlamellar spacing of 0.38 nm, while no carbon nanoparticles were observed. Certain bamboo-like structures were discovered in the hollow core of the CNTs. These structures are generated in the growing process of CNTs. Carbon atoms from ethanol dissolve into the high-heat copper catalyst and form a carbon-copper alloy until saturated. Then the carbon atoms separate from the alloy to the surface and continues to push up, in which the bamboo-like structures are introduced in the grown CNTs [29,30]. These CNTs are mainly formed in base-growth mode due to the strong combination force between catalyst copper and silicon substrate. Fig. 2j captured a CNT separating out of a copper catalyst particle, which evidenced the base-growth mechanism. From Fig. 2k, the key role of the coper particles can be clearly understood. On one hand, the copper nanoparticle anchors on PMSi tightly; On the other hand, one end of the CNT embraces the copper nanoparticle closely. Thus, perfect electrical and mechanical contact are formed, even high-energy ultrasonic dispersion cannot separate them.

X-ray diffraction patterns (Fig. 3a) and Raman spectra (Fig. 3b) were collected. As comparison, a composite that PMSi mixed with commercial CNTs (CCT) and covered with a carbon layer (PMSi/CCT/C) was prepared and tested. As shown in Fig. 3a, three strong X-ray diffraction peaks for PMSi are identified to be Si (111), Si (220), and Si (311). After Cu particles dispersion (PMSi/Cu) by thermal reduction process of Cu $(NO_3)_2$ in Ar/H_2 atmosphere at 580 °C, two small peaks at 43.38° and 50.05° appears, which are ascribed to metallic Cu (111) and Cu (220). Because of the solid-phase reaction between silicon and Cu nano-particle at high temperature, two weak peaks of Cu_3Si at 44.58° and 44.99° are also observed. After CNTs growth (PMSi/CNT/C) in 800 °C, the peaks of Cu and Cu_3Si become clearer and stronger. In addition, a weak peak ascribed to carbon (002) crystal plane at 25.66 emerges. It's worth noting that the formation of Cu_3Si is crucial for the structural stability of PMSi/CNT/C in battery cycling. The Cu_3Si silicide is inactive towards lithium so that the Cu_3Si patches bond tightly to PMSi and reinforce the secondary structure in the following charge and discharge process [31]. The adhesion property of the Cu_3Si is very effective to ensure intimate mechanical contact between the PMSi particle, unreacted Cu-catalyst, and the grown CNTs. The conductive Cu_3Si and the residual Cu particles on the Si surface supply electrical conducting channels and well distributed electric field, which can depress the cross potential aroused by polarization [32,33]. In this work, only 0.028 wt‰ Cu nano-particles are adopted as catalyst in PMSi to grow CNTs. Although the residual Cu particles are inactive towards lithium, the loss of capacity is very little and negligible. The XRD curve of PMSi/CNT/C and PMSi/CCT/C didn't appear new crystallization peak, demonstrating an amorphous carbon structure of the carbon layer generated from PAN during carbonization process. X-ray diffraction patterns of Cu current collector before and after heating were also collected (Figure S2 a). All peaks become a little sharper after heating, indicating a better crystallization. Meanwhile, from I–V test (Figure S2 b), the resistance of heated Cu current collector

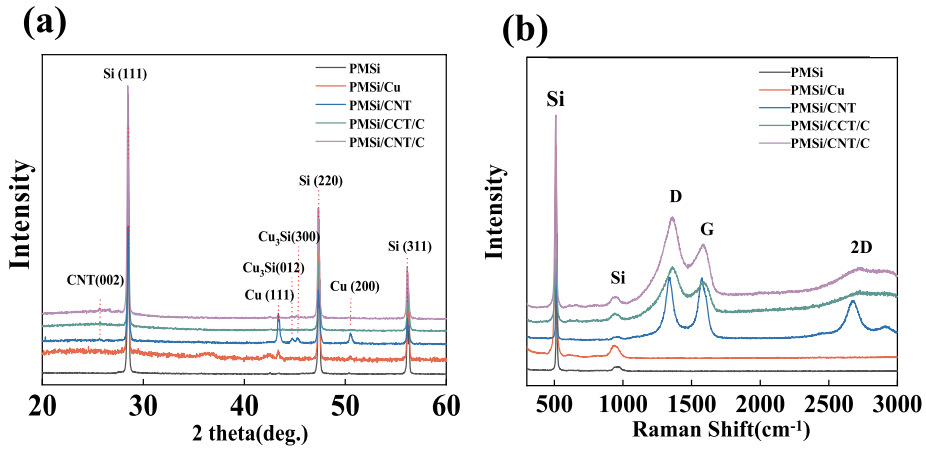

Fig. 3. X-ray diffraction patterns (a) and Raman spectra (b) of the PMSi, PMSi/Cu, PMSi/CNT, PMSi/CCT/C, PMSi/CNT/C.

is less than that before heating. In this sense, the impact of heating Cu current collector is positive.

In the Raman spectra shown in Fig. 3b, two peaks at 520 cm^{-1} and 1040 cm^{-1} are from PMSi, which represents the vibration of crystalline silicon and the second-order optical phonons vibrations of Si–Si bands, respectively. No new peaks are observed for PMSi/Cu while four new peaks from multi-wall CNTs for PMSi/CNT appear. They are assigned to be the D peak (1342 cm^{-1}), G peak (1575 cm^{-1}), 2D peak (2726 cm^{-1}) and the –CH peak (2913 cm^{-1}). The D peak represents the breathing vibration mode of sp [2] hybridized carbon atom rings in CNT, which is activated by the defects and disorder of carbon lattice. The G peak is due to a bond stretching vibration of a pair of sp [2] sites corresponding to graphitic cluster lattice vibration mode. The intensity ratio of the D band to the G band was 0.896, indicating that the obtained CNTs are relatively pure except several defects formed during the growing process. The peak at 2913 cm^{-1} was caused by –CH aliphatic stretching [34,35], which is

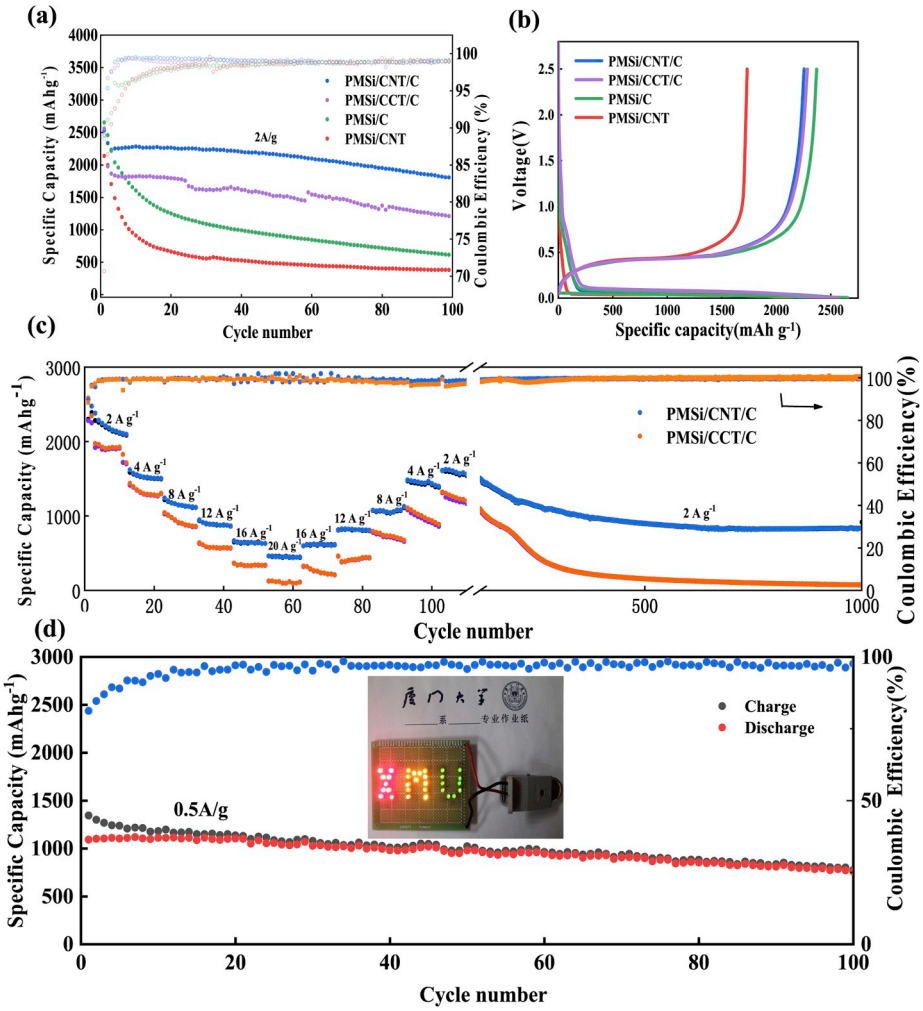

Fig. 4. (a) Specific capacity comparison of PMSi/CNT/C, PMSi/CCT/C, PMSi/C, and PMSi/CNT at 2 A g^{-1} between 0.005 V and 2.5 V for 100 cycles. (b) Corresponding galvanostatic charge–discharge profiles at the 1st cycle. (c) Rate performance of the PMSi/CNT/C and PMSi/CCT/C electrodes at various rates from 2 A g^{-1} to 20 A g^{-1} for 1000 cycles. (All the electrodes were test at current densities of 0.2 A g^{-1} for the first two cycles.) (d) Cycling performance of the full cell (N/P ratio = 1.1) between 2.8 V and 3.9 V containing $LiFePO_4/LiMn_2O_4$ cathode (2.5 mAh cm^{-2}) and PMSi/CNT/C anode (2.75 mAh cm^{-2}). Inset: A full cell successfully ignites the LED array (~1.5 W).

probably introduced by pyrolysis product of ethanol. After carbon coated, the PMSi/CNT/C and PMSi/CCT/C composite reveal similar peak curves. The D peak of carbon gets stronger, indicating that plenty of defects consist in the carbon layer, which is in accordance with the XRD results.

Cycling performance of PMSi/CNT/C, PMSi/CCT/C, and PMSi/C (without CNTs additive) at 2 A g^{-1} was measured respectively in a coin-cell configuration with a lithium metal as the counter electrode in Fig. 4a. The corresponding galvanostatic charge/discharge profile for the first cycle is exhibited in Fig. 4b. All the electrodes were first tested at a rate of 0.2 A g^{-1} for two cycles and all reported specific capacities are based on the total mass of the composite electrode material. The PMSi/CNT/C electrode exhibited an outstanding performance, retaining a specific capacity of 1803 mAh g^{-1} after 100 cycles. In contrast, the PMSi/CCT/C electrode had a marked capacity decay with only 1211 mAh g^{-1} retained, demonstrating a serious electrode polarization and poor stability. It is indicated that simply mixing CNT into electrode materials does not obviously improve the electrode stability. An unexpected thermostat (30 °C) failure caused some discontinuity for the cycling curve of PMSi/CCT/C, which did not affect our forecasting and analysis of the overall trend and we did not retest it. As for the PMSi/C, polarization and instability of the electrode are even more serious. Moreover, an extra contrast experiment of PMSi/CNT electrode (CNT grown on PMSi without C coated; CMC and carbon black were used as adhesives and conductive agents respectively) was carried out to further elaborates the role of the carbon layer. It is observed that PMSi/CNT electrode delivers the worst cycling performance. The specific battery capacity severely attenuates from 2038 mAh g^{-1} to 866 mAh g^{-1} during the first 10 cycles. We ascribe this capacity attenuation to the direct contact between silicon anode and electrolyte during repeated lithiation/delithiation processes, which led to violent side-effects and continuous formation of an unstable SEI. It appears to us that a carbon layer is irreplaceable since slight meshy fabric of CNT fails to serve as a stable cladding.

In Fig. 4b, all the curves in the first charge exhibits a plateau at ~80 mv, indicating an intercalation of lithium into crystalline silicon. The PMSi/CNT/C composite delivered an initial charge/discharge capacity of 2256 mAh g^{-1} and 2533 mAh g^{-1} with a high first cycle coulombic efficiency (CE) of 89.07%. Irreversible capacity loss at first cycle is related to the formation of SEI and the defects in the carbon layer. The high CE is attributed to the lower specific surface area and less irreversible consumption of Li^+. After a few cycles, the CE is measured exceeding 99%. This indicates that a stable SEI layer has formed outside the carbon layer during the initial cycles and renders an active surface substantially inert to further electrolyte decomposition. The total irreversible capacity loss ratio at the first 10, 20th and 50th cycles is 2.5%, 3.38% and 7.4%. PMSi/CCT/C shows a similar level as PMSi/CNT/C, while PMSi/CNT demonstrates the lowest CE and initial charge capacity, and PMSi/C demonstrates the best. The sacrificed capacity of PMSi/CNT/C and PMSi/CCT/C relative to PMSi/C is considered to be caused by the small quantity of CNTs with large specific surface area which slightly increase the first irreversible capacity [36–38].

Rate capability of the PMSi/CNT/C and the PMSi/CCT/C electrode were also evaluated in Fig. 4c with a stepwise current density programmed from 2 to 20 A g^{-1}. The specific capacity decreases with the increase of the current density along the steps. The discharge capacities of PMSi/CNT/C for the first cycle at these rates are 2383, 1620, 1243, 949, 668, 463 mAh g^{-1} at 2, 4, 8, 12, 16, and 20 A g^{-1}, respectively, which are stable with the minor changes at the same current density. When the current density is set back, the capacity can recover to a similar value. Over 840 mA h g^{-1} for 1000 cycles at 2 A g^{-1} was measured in the end. The electrode remains a stable cycling at different current densities and long cycle, demonstrating the excellent rate capability and reversibility of the PMSi/CNT/C electrode. In our case, PMSi/CCT/C electrode shows a great polarization effect in rate test and the capacity fades drastically below 200 mAh g^{-1} after the 300th cycle.

Additionally, full cells with the PMSi/CNT/C anode and a $LiFePO_4$/$LiMn_2O_4$ cathode were assembled to test its electrical performance in practical application. Considering the low initial coulombic efficiency of about 74.21%, the PMSi/CNT/C electrode was first prelithiated using half cells at 0.2 A g^{-1} for two cycles to form a stable SEI. The full cell with an N/P ratio of 1.1 was tested at 0.5 A g^{-1} in Fig. 4d. High discharge specific capacity of 1093.1 mAh g^{-1} with an initial coulombic efficiency of 81.26% and an 80% capacity retention at the 77th cycle is measured. The initial thickness of the electrode is measured to be 27 μm while the electrode expands to 33 μm after the first lithiation process. The volume expansion ratio is calculated to be 22% (Fig. S3). As is shown in the inset of Fig. 4d, the full cell successfully ignites a LED array of the logo "XMU" with 1.5 W rated power, demonstrating the outstanding driving performance in practical application. Detail process can be found in Fig. S4.

To confirm the stable electrode structure and robust CNT networks of PMSi/CNT/C, the coin half-cells containing PMSi/CNT/C and PMSi/CCT/C, respectively, cycled between 0.05 and 1.0 V at 2 A g^{-1} were disassembled after 100 cycles. Benefiting from the CNTs that evenly dispersed and embedded in the carbon layer, the cycled PMSi/CNT/C electrode remains structurally intact without severe cracks (Fig. 5a). From the high magnification morphology of crevice in Fig. 5b, though a SEI layer is generated and covers the electrode, CNTs are vaguely seen to connect across inter-particles. Nevertheless, cracks were clearly found in cycled PMSi/CCT/C electrode (Fig. 5 c-d). The ability of easily agglomerated commercial CNTs to improve electrode structural stability is limited. Additional evidence for tightly fastened CNT is presented. Considering the complex characterization of morphology for cycled silicon powder, a silicon wafer was selected as a substrate to disperse Cu nano-particles and grow CNTs (Figure S5 a). The silicon wafer was then cut into small pieces and assembled in a CR2025 coin half-cell with a lithium foil. SEM images of the wafer after 5 lithiation/delithiation processes are provided in Fig. S5 b and Fig. S5 c. Despite the drastic expansion and shrink of silicon wafer, the ends of CNTs are not separated from the white dots (Cu particles), which demonstrates the tightly fastened CNT.

Considering in PMSi/CNT/C composite, the CNTs were grown directly on the PMSi and the connection type between CNTs and PMSi is different from the PMSi/CCT/C. In order to investigate the key role of

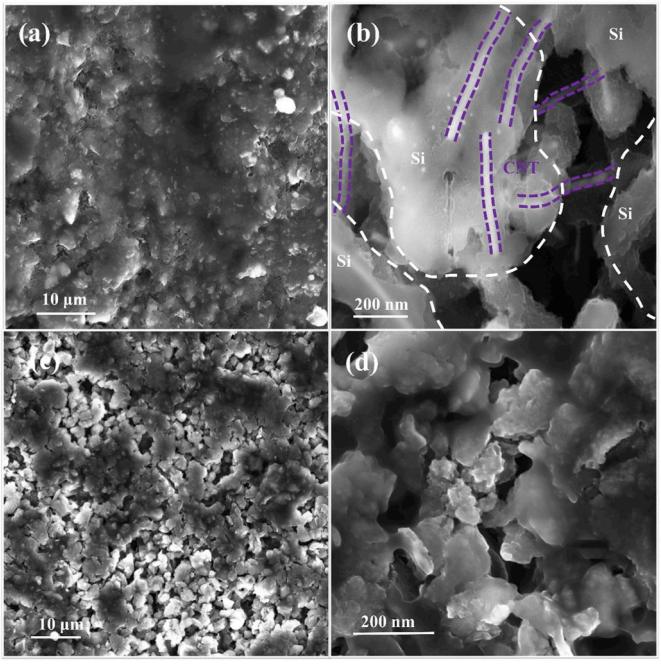

Fig. 5. SEM images of the PMSi/CNT/C (a, b) and PMSi/CCT/C electrodes (c, d) after 100 cycles between 0.05 V and 2.5 V.

the two different CNT conductive networks in improving the rate performance, we measured the electrochemical impedance spectroscopy (EIS) of PMSi/C, MSi/CCT/C, and PMSi/CNT/C at the state of charge (SOC) of 50% after 5 cycles (Fig. 6a). All the plot of PMSi/C exhibit the combination of an incomplete semicircle at the medium-high frequency region (Cut-off frequency at 68.13 Hz) and a slope line at the low frequency, while the plots of PMSi/CCT/C and PMSi/CNT/C exhibit one more semicircle at the medium frequency region with similar cut-off frequencies of 0.825 Hz and 1 Hz respectively. Since the CNTs possess a high specific surface area of 250–270 $m^2\ g^{-1}$, we attribute the extra semicircle to the large interface layer introduced by CNTs [39,40]. The Nyquist plots were fitted with an equivalent circuit (Fig. 6a insets) and the fitting parameters are list in Fig. 6b. R_1 represents the resistance of the electron transport and the Li^+ diffusion in electrolyte [41]. As can be seen, the R_1 is similarly low for all. However, the PMSi/CNT/C anode exhibits a much smaller resistances of charge transfer and SEI layer (R_2 = 9.61 Ω) as compared to the PMSi/C anode (R_2 = 18.42 Ω) and the PMSi/CCT/C anode (R_2 = 18.34 Ω). In Fig. 6c, by linear fitting of Z_{real} versus $\omega^{-1/2}$, the slope values of B can be extracted. B is considered to be a constant which associates with the diffusion coefficient D of Li^+ inside the electrode materials. The relationship is expressed by formula $B = -V_m \cdot (2\ F\ A \cdot D)^{-1/2} \cdot dE/dx$, where V_m is molar volume of sample, F is faraday constant, and dE/dx is slope of coulomb titration curve [42,43]. From Fig. 6c, the plot slopes of PMSi/C, PMSi/CCT/C, PMSi/CNT/C are calculated as 31.53, 9.27, and 3.51 respectively, indicating PMSi/CNT/C possesses a higher Li^+ diffusion coefficient, which is 7 times of PMSi/CCT/C and 80 times of PMSi/C. For mixed ion and electron conductors (lithium silicon alloy), strong interaction exists between Li^+ ions and electrons. The transport of Li^+ ions is intimately linked to the transport of electrons [44,45]. So a high-efficiency electron transport route may also improve the ionic conductivity.

On the other hand, to further evaluate the separate electronic components of the total charge transport in mixed ionic and electronic solids [46], we carried out IV characterization. The PMSi, PMSi/CCT, and PMSi/CNT composites were pressed by hydraulic machine into thin films on which copper pads were sputtered (Fig. 6d). Expectedly, with the addition of CNTs, bulk resistance of PMSi significantly reduced and the corresponding current increased by almost three orders of magnitude at the same excitation voltage (Fig. 6e). The resistivity of PMSi, PMSi/CCT, and PMSi/CNT are calculated to be 88136 Ω m, 400 Ω m, and 157 Ω m, respectively. Owing to the unique contact structure of CNT network and silicon, the PMSi/CNT exhibits the smallest inter-particle resistances, which is of great significance to reduce polarization and improve the rate performance in practical application.

The contact resistance between silicon and copper may further decreases after annealing due to formation of Cu_3Si silicide inter-junctions. To verify this, IV characterization curve (Fig. 6f) of the PMSi thin film with copper electrodes was examined before and after annealing in an argon atmosphere at 800 °C. Considering that bulk-resistance of PMSi thin film may also change during annealing process, a comparison experiment was added that the PMSi thin film was pre-annealed before copper electrodes sputtering. With forward bias, the sample annealed after sputtering showed the highest conductivity. The slight asymmetry with forward and backward biases of the IV curves is caused by the metal-semiconductor rectifying contact [47,48].

Overall, we successfully innovated the connection type of PMSi-CNT instead of simply mixing them. The grown CNTs using CVD method take root in the surface of the silicon particle through Cu_3Si silicide formation, exerting its ability to conduct electricity at the greatest extent. The Cu_3Si silicide, working as a joint, offers excellent mechanical stability as well as conductivity owing to its chemical inertness during battery operation. Meanwhile, CNTs give excellent mechanical strength and suppleness, which supply a self-adapted electronic network to resist the severe volume changes during cycling. Even if mechanical fracture of PMSi occurred in the subsequent battery cycle process, CNTs did not detach from the silicon particles. And by sustaining robust electrical conductivity in and inter silicon particles through the CNTs, electrons are capable of migrating to each silicon particle directly and credibly.

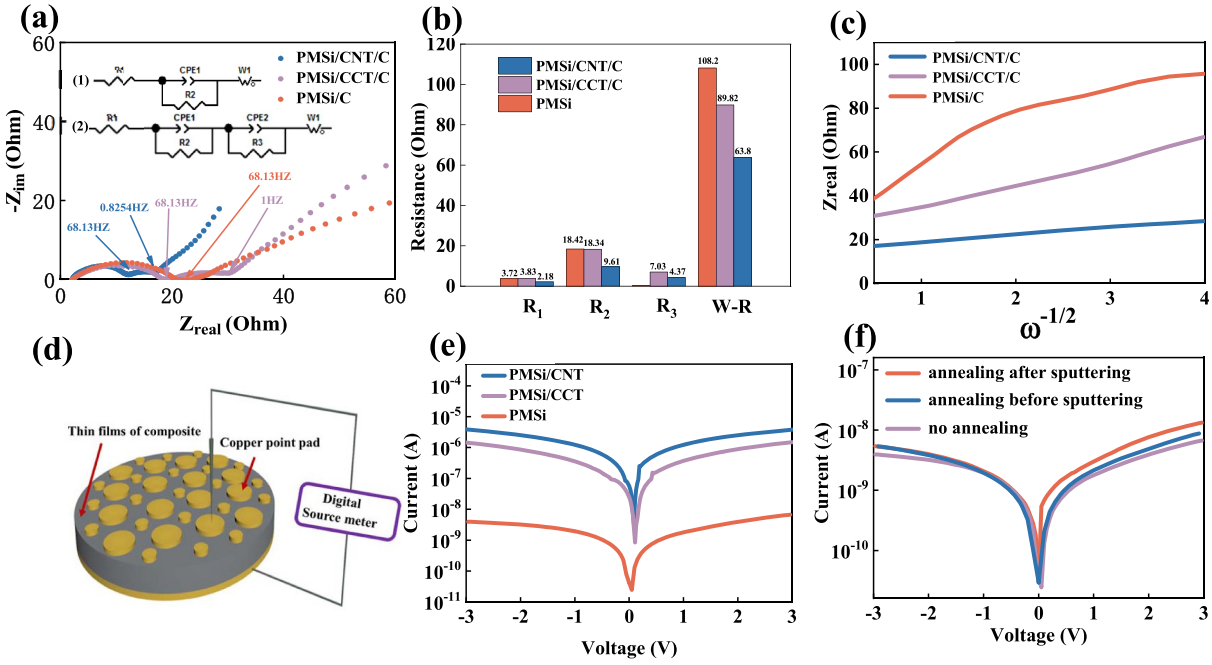

Fig. 6. (a) Electrochemical impedance spectrum with frequency ranging from 100 kHz to 0.01 Hz. Insets: (1) Equivalent circuit of the PMSi/C electrode. (2) Equivalent circuit of the PMSi/CNT/C and the PMSi/CCT/C electrode. (b) Fitting results of the PMSi, PMSi/CCT/C, and PMSi/CNT/C composite electrodes. (c) Relationship between Z_{real} and $\omega^{-1/2}$ with frequency range from 10 Hz to 0.01 Hz. (d) Sketch diagram of IV testing process. PMSi/CNT, PMSi/CCT, and PMSi composites are pressed into thin films (10 mm in diameter and 1 mm in thickness) with several copper point pads (500 μm in diameter) and a copper back pad. (e) IV characteristics of PMSi, PMSi/CCT, and PMSi/CNT composites. (f) IV characteristics of copper-silicon contact impedance before and after annealing in 800 °C. (For interpretation of the references to colour in this figure legend, the reader is referred to the Web version of this article.)

Such a high-efficiency electron conducting network improves Li^+ ionic conductivity at the same time. As a result, both Li^+ and electron obtained high mobility. While for traditional structure the active material and CNTs are simply physically stacked together. The loose and vulnerable contacts between CNTs and the particles means that once the anode structure are deformed or fractured during the charge-discharge process, electrons have to transfer through numerous particles and led to large bulk resistance. Additional carbon shielding is also necessary to enforce the network. As shown by our experiment, anode using MSi mixed with commercial CNTs suffered from poor structural stability problem.

3. Conclusion

A novel PMSi/CNT/C composite has been synthesized as LIB anode taking advantage of the intimate contacts between grown CNTs and PMSi. This unique structure not only exert mechanical stability, but also provide high mobility of both Li^+ and electron. Therefore, it is attractive to meet the demand of long life cycles at high rate for practical application. Safety, simple synthesis process, and low cost are also important considerations for industrial employments. In addition, this design idea can be expanded in other similar areas that suffer from low conductivity or poor mechanical stability.

4. Experimental section

4.1. Synthesis of PMSi/CNT

Typically, 3 g of MSi were treated by a solution of 20 mM $CuSO_4$ and 2.5 M HF (diluted by 300 ml deionized water and 100 ml ethanol) at 80 °C for 12 h to gain PMSi. The as-obtained PMSi were completely immersed in concentrated nitric acid at room temperature for 1 h to remove Cu. The PMSi were then filtered, washed, dipped in a solution of $Cu(NO_3)_2$ (1 ML^{-1}) for 5 min, filtered again, and dried in vacuum at 80 °C so that $Cu(NO_3)_2$ nano-particles were evenly dispersed in the potholes of PMSi. Then the PMSi were transported to a quartz-tube furnace and heated to 580 °C with a ramping rate of 5 °C min^{-1} in Ar/H_2 atmosphere (200 sccm). The annealing treatment lasted 30 min to fully reduce the $Cu(NO_3)_2$ to metallic copper nano-particles. Then using Ar/H_2 as carrier gas (200 sccm), ethanol vapor was introduced into the furnace. At the same time, the furnace was immediately heated to 800 °C and kept for 1 h.

4.2. Fabrication of PMSi/CNT/C electrodes

100 mg of the PMSi/CNT powder was ball milled with 500 mg of a PAN solution (10 wt% dissolved in DMF) for 1 h at 200 rpm. Following this, the mixed slurry was spread onto copper foil as a current collector with a diameter of 14 mm and dried. The as-obtained electrodes were then heated to 700 °C in Ar/H_2 atmosphere for 1 h with a ramping rate of 5 °C min^{-1} without use of any binder or conductive agent. The mass loading per electrode is 1.2–1.5 mg.

4.3. Characterization

The obtained samples were characterized by Scanning electron microscopy (SEM, Hitachi S4800,15 KV), transmission electron microscopy (TEM, Philips Tecnai F30), X-ray diffraction (Rigaku Ultima IV with Cu Ka radiation), Raman spectroscopy (WITEC $\lambda = 488$ nm). A Vario EL III (Elementar, Germany) was used to analyze the elemental content. The Brunauer Emmett Teller (BET) specific surface area of the samples was determined by an ariStar II surface area and porosity system using the standard N_2 adsorption and desorption isotherm measurements at 77 K. The active mass was weighted by a microbalance (METTLER TOLEDO XS3DU). IV characteristics are measured by a digital Source-Meter (Keithley, 2611 B).

4.4. Electrochemical test

The CR2025 coin half-cell with a lithium foil assembled in an argon-filled glove box (MBRAUN, LABmaster 100, Germany), were used to test the electrochemical performance. The electrolyte solution was 1 M $LiPF_6$ in ethylene carbonate (EC), dimethyl carbonate (DMC) and diethyl carbonate (DEC) (1:1:1 in volume) with 10% fluorinated ethylene carbonate (FEC) additive. The cells were tested over a voltage range of 0.005–2.5 V (versus Li^+/Li) at room temperature using a Land CT2001A system (Wuhan, China). EIS was performed from 100 kHz to 10 mHz with 10 mV of amplitude on an electrochemical workstation (Shanghai Chenhua, CHI 660 E). The full cells designed with an N/P ratio of 1.1 (Anode with area capacity of 2.75 mAh cm^{-2} and cathode with area capacity of 2.5 mAh cm^{-2} were designed), were carried out in the voltage window between 2.8 V and 3.9 V. The thickness, mass loading and diameter of the anode electrode is 27 μm, 2.68 mg and 14 mm, respectively. The PMSi/CNT/C anode was first prelithiated using half cells at 0.2 Ag^{-1} for two cycles to form a stable SEI. The cathode electrode material consists of $LiFePO_4$, $LiMn_2O_4$, SP, Ls-6, PVDF (70:20:2:2:6) was purchased from the Fast-Pass company.

Powders of PMSi, PMSi/CCT, PMSi/CNT were pressed into round thin films (10 mm in diameter and 1 mm in thickness) by hydraulic machine at the pressure of 25 kg cm^{-2}. These films were then sputtered with several copper point pads (500 μm in diameter) and a copper back pad using magnetron sputtering equipment (SKY Technology Development Co.Ltd Chinese Academy of Sciences) (current 3.0 A, Argon flow rate 22 sccm).

Declaration of competing interest

The authors declare that they have no known competing financial interests or personal relationships that could have appeared to influence the work reported in this paper.

Acknowledgements

Financial support from the National Natural Science Foundation of China (Grants 61534005, 21761132030), General Armaments Department, People's Liberation Army of China (6140721040411), Natural Science Foundation of Jiangxi Province (20192ACBL20048) are acknowledged.

Appendix A. Supplementary data

Supplementary data to this article can be found online at https://doi.org/10.1016/j.jpowsour.2019.227593.

References

[1] A. Magasinski, P. Dixon, B. Hertzberg, A. Kvit, J. Ayala, G. Yushin, High-performance lithium-ion anodes using a hierarchical bottom-up approach, Nat. Mater. 9 (4) (2010) 353–358, https://doi.org/10.1038/nmat2725.
[2] M. Armand, J.M. Tarascon, Building better batteries, Nature 451 (7179) (2008) 652–657, https://doi.org/10.1038/451652a.
[3] F.M. Hassan, V. Chabot, A.R. Elsayed, X. Xiao, Z. Chen, Engineered Si electrode nanoarchitecture: a scalable postfabrication treatment for the production of next-generation Li-ion batteries, Nano Lett. 14 (1) (2014) 277–283, https://doi.org/10.1021/nl403943g.
[4] P. Simon, Y. Gogotsi, Materials for electrochemical capacitors, Nat. Mater. 7 (11) (2008) 845–854, https://doi.org/10.1038/nmat2297.
[5] B. Kang, G. Ceder, Battery materials for ultrafast charging and discharging, Nature 458 (7235) (2009) 190–193, https://doi.org/10.1038/nature07853.
[6] M.T. McDowell, S.W. Lee, W.D. Nix, Y. Cui, 25th anniversary article: understanding the lithiation of silicon and other alloying anodes for lithium-ion batteries, Adv. Mater. 25 (36) (2013) 4966–4984, https://doi.org/10.1002/adma.201301795.
[7] M. Chen, B. Li, X.J. Liu, L. Zhou, L. Yao, J.T. Zai, X.F. Qian, X.B. Yu, Boron-doped porous Si anode materials with high initial coulombic efficiency and long cycling stability, J. Mater. Chem. 6 (7) (2018) 3022–3027, https://doi.org/10.1039/c7ta10153h.

[8] M. Ashuri, Q.R. He, L.L. Shaw, Silicon as a potential anode material for Li-ion batteries: where size, geometry and structure matter, Nanoscale 8 (1) (2016) 74–103, https://doi.org/10.1039/c5nr05116a.
[9] H. Wu, Y. Cui, Designing nanostructured Si anodes for high energy lithium ion batteries, Nano Today 7 (5) (2012) 414–429, https://doi.org/10.1016/j.nantod.2012.08.004.
[10] L.H. Liu, J. Lyu, T.H. Li, T.K. Zhao, Well-constructed silicon-based materials as high-performance lithium-ion battery anodes, Nanoscale 8 (2) (2016) 701–722, https://doi.org/10.1039/c5nr06278k.
[11] T. Kennedy, M. Brandon, K.M. Ryan, Advances in the application of silicon and germanium nanowires for high-performance lithium-ion batteries, Adv. Mater. 28 (27) (2016) 5696–5704, https://doi.org/10.1002/adma.201503978.
[12] S. Suresh, Z.P. Wu, S.F. Bartolucci, S. Basu, R. Mukherjee, T. Gupta, P. Hundekar, Y.F. Shi, T.M. Lu, N. Koratkar, Protecting silicon film anodes in lithium-ion batteries using an atomically thin graphene drape, ACS Nano 11 (5) (2017) 5051–5061, https://doi.org/10.1021/acsnano.7b01780.
[13] Z.D. Lu, N. Liu, H.W. Lee, J. Zhao, W.Y. Li, Y.Z. Li, Y. Cui, Nonfilling carbon coating of porous silicon micrometer-sized particles for high-performance lithium battery anodes, ACS Nano 9 (3) (2015) 2540–2547, https://doi.org/10.1021/nn505410q.
[14] H. Wu, G. Chan, J.W. Choi, I. Ryu, Y. Yao, M.T. McDowell, S.W. Lee, A. Jackson, Y. Yang, L. Hu, Y. Cui, Stable cycling of double-walled silicon nanotube battery anodes through solid-electrolyte interphase control, Nat. Nanotechnol. 7 (5) (2012) 310–315, https://doi.org/10.1038/nnano.2012.35.
[15] Q. Zhang, H. Chen, L. Luo, B. Zhao, H. Luo, X. Han, J. Wang, C. Wang, Y. Yang, T. Zhu, M. Liu, Harnessing the concurrent reaction dynamics in active Si and Ge to achieve high performance lithium-ion batteries, Energy Environ. Sci. 11 (3) (2018) 669–681, https://doi.org/10.1039/c8ee00239h.
[16] B.M. Bang, H. Kim, H.-K. Song, J. Cho, S. Park, Scalable approach to multi-dimensional bulk Si anodes via metal-assisted chemical etching, Energy Environ. Sci. 4 (12) (2011) 5013–5019, https://doi.org/10.1039/c1ee02310a.
[17] X. Huang, J. Yang, S. Mao, J. Chang, P.B. Hallac, C.R. Fell, B. Metz, J. Jiang, P. T. Hurley, J. Chen, Controllable synthesis of hollow Si anode for long-cycle-life lithium-ion batteries, Adv. Mater. 26 (25) (2014) 4326–4332, https://doi.org/10.1002/adma.201400578.
[18] P. Avouris, J. Appenzeller, R. Martel, S.J. Wind, Carbon nanotube electronics, Proc. IEEE 9 (11) (2003) 1772–1784, https://doi.org/10.1109/jproc.2003.818338.
[19] H. Cai, K. Han, H. Jiang, J. Wang, H. Liu, Self-standing silicon-carbon nanotube/graphene by a scalable in situ approach from low-cost Al-Si alloy powder for lithium ion batteries, J. Phys. Chem. Solids 109 (2017) 9–17, https://doi.org/10.1016/j.jpcs.2017.05.009.
[20] D.N. Ho, O. Yildiz, P. Bradford, Y. Zhu, P.S. Fedkiw, A silicon-impregnated carbon nanotube mat as a lithium-ion cell anode, J. Appl. Electrochem. 48 (1) (2017) 127–133, https://doi.org/10.1007/s10800-017-1140-8.
[21] T. Kowase, K. Hori, K. Hasegawa, T. Momma, S. Noda, A-few-second synthesis of silicon nanoparticles by gas-evaporation and their self-supporting electrodes based on carbon nanotube matrix for lithium secondary battery anodes, J. Power Sources 363 (2017) 450–459, https://doi.org/10.1016/j.jpowsour.2017.07.115.
[22] Y. Yang, X. Yang, S. Chen, M. Zou, Z. Li, A. Cao, Q. Yuan, Rational design of hierarchical carbon/mesoporous silicon composite sponges as high-performance flexible energy storage electrodes, ACS Appl. Mater. Interfaces 9 (27) (2017) 22819–22825, https://doi.org/10.1021/acsami.7b05032.
[23] J.C. Charlier, A. DeVita, X. Blase, R. Car, Microscopic growth mechanisms for carbon nanotubes, Science 275 (5300) (1997) 646–649.
[24] L.F. Sun, J.M. Mao, Z.W. Pan, B.H. Chang, W.Y. Zhou, G. Wang, L.X. Qian, S.S. Xie, Growth of straight nanotubes with a cobalt-nickel catalyst by chemical vapor deposition, Appl. Phys. Lett. 74 (5) (1999) 644–646, https://doi.org/10.1063/1.123027.
[25] X. Han, Z. Zhang, R. You, G. Zheng, C. Li, S. Chen, Y. Yang, Capitalization of interfacial AlON interactions to achieve stable binder-free porous silicon/carbon anodes, J. Mater. Chem. 6 (17) (2018) 7449–7456, https://doi.org/10.1039/c8ta01029c.
[26] X. Han, H. Chen, Z. Zhang, D. Huang, J. Xu, C. Li, S. Chen, Y. Yang, Carbon-coated Si micrometer particles binding to reduced graphene oxide for a stable high-capacity lithium-ion battery anode, J. Mater. Chem. 4 (45) (2016) 17757–17763, https://doi.org/10.1039/c6ta07274g.
[27] X. Han, H. Chen, X. Li, J. Wang, C. Li, S. Chen, Y. Yang, Interfacial nitrogen stabilizes carbon-coated mesoporous silicon particle anodes, J. Mater. Chem. 4 (2) (2016) 434–442, https://doi.org/10.1039/c5ta08297h.
[28] X. Han, H. Chen, J. Liu, H. Liu, P. Wang, K. Huang, C. Li, S. Chen, Y. Yang, A peanut shell inspired scalable synthesis of three-dimensional carbon coated porous silicon particles as an anode for lithium-ion batteries, Electrochim. Acta 156 (2015) 11–19, https://doi.org/10.1016/j.electacta.2015.01.051.
[29] Y.H. Wang, M.J. Kim, H.W. Shan, C. Kittrell, H. Fan, L.M. Ericson, W.F. Hwang, S. Arepalli, R.H. Hauge, R.E. Smalley, Continued growth of single-walled carbon nanotubes, Nano Lett. 5 (6) (2005) 997–1002, https://doi.org/10.1021/nl047851f.
[30] J.C. Charlier, H. Amara, P. Lambin, Catalytically assisted tip growth mechanism for single-wall carbon nanotubes, ACS Nano 1 (3) (2007) 202–207, https://doi.org/10.1021/nn700049q.
[31] S. Chae, M. Ko, S. Park, N. Kim, J. Ma, J. Cho, Micron-sized Fe–Cu–Si ternary composite anodes for high energy Li-ion batteries, Energy Environ. Sci. 9 (4) (2016) 1251–1257, https://doi.org/10.1039/c6ee00023a.
[32] Z. Zheng, H.H. Wu, H. Chen, Y. Cheng, Q. Zhang, Q. Xie, L. Wang, K. Zhang, M. S. Wang, D.L. Peng, X.C. Zeng, Fabrication and understanding of Cu3Si-Si@carbon@graphene nanocomposites as high-performance anodes for lithium-ion batteries, Nanoscale 10 (47) (2018) 22203–22214, https://doi.org/10.1039/c8nr07207h.
[33] H. Chen, Y. Xiao, L. Wang, Y. Yang, Silicon nanowires coated with copper layer as anode materials for lithium-ion batteries, J. Power Sources 196 (16) (2011) 6657–6662, https://doi.org/10.1016/j.jpowsour.2010.12.075.
[34] T.C. Chung, Y. Schlesinger, S. Etemad, A.G. Macdiarmid, A.J. Heeger, Optical studies OF pyrolyzed polyacrylonitrile, J. Polym. Sci. B Polym. Phys. 22 (7) (1984) 1239–1246, https://doi.org/10.1002/pol.1984.180220708.
[35] X. Gi, J. Dong, J.F. Zhang, Sers studies OF polymers ON metal-surfaces .4. Cyclization and graphitization OF polyacrylonitrile ON rough silver surfaces, Macromolecules 25 (21) (1992) 5855–5857.
[36] W. Wang, P.N. Kumta, Nanostructured hybrid silicon/carbon nanotube heterostructures: reversible high-capacity lithium-ion anodes, ACS Nano 4 (4) (2010) 2233–2241, https://doi.org/10.1021/nn901632g.
[37] Q.Z. Xiao, Y. Fan, X.H. Wang, R.A. Susantyoko, Q. Zhang, A multilayer Si/CNT coaxial nanofiber LIB anode with a high areal capacity, Energy Environ. Sci. 7 (2) (2014) 655–661, https://doi.org/10.1039/c3ee43350a.
[38] W. Wang, I. Ruiz, K. Ahmed, H.H. Bay, A.S. George, J. Wang, J. Butler, M. Ozkan, C.S. Ozkan, Silicon decorated cone shaped carbon nanotube clusters for lithium ion battery anodes, Small 10 (16) (2014) 3389–3396, https://doi.org/10.1002/smll.201400088.
[39] H. Huang, W. Zhang, M. Li, Y. Gan, J. Chen, Y. Kuang, Carbon nanotubes as a secondary support of a catalyst layer in a gas diffusion electrode for metal air batteries, J. Colloid Interface Sci. 284 (2) (2005) 593–599, https://doi.org/10.1016/j.jcis.2004.10.067.
[40] D. Thiele, A. Züttel, Electrochemical characterisation of air electrodes based on La0.6Sr0.4CoO3 and carbon nanotubes, J. Power Sources 183 (2) (2008) 590–594, https://doi.org/10.1016/j.jpowsour.2008.05.042.
[41] B.-A. Mei, O. Munteshari, J. Lau, B. Dunn, L. Pilon, Physical interpretations of nyquist plots for EDLC electrodes and devices, J. Phys. Chem. C 122 (1) (2017) 194–206, https://doi.org/10.1021/acs.jpcc.7b10582.
[42] B. Wang, T. Liu, A. Liu, G. Liu, L. Wang, T. Gao, D. Wang, X.S. Zhao, A hierarchical porous C@LiFePO4/carbon nanotubes microsphere composite for high-rate lithium-ion batteries: combined experimental and theoretical study, Adv. Energy Mater. 6 (16) (2016), https://doi.org/10.1002/aenm.201600426.
[43] S. Wang, J. Liao, M. Wu, Z. Xu, F. Gong, C. Chen, Y. Wang, X. Yan, High rate and long cycle life of a CNT/rGO/Si nanoparticle composite anode for lithium-ion batteries, Part. Part. Syst. Charact. 34 (10) (2017), https://doi.org/10.1002/ppsc.201700141.
[44] R.C. Agrawal, R.K. Gupta, Superionic solids: composite electrolyte phase - an overview, J. Mater. Sci. 34 (6) (1999) 1131–1162, https://doi.org/10.1023/a:1004598902146.
[45] D.K. Lee, H.I. Yoo, Electron-ion interference and onsager reciprocity in mixed ionic-electronic transport in TiO2, Phys. Rev. Lett. 97 (25) (2006) 4, https://doi.org/10.1103/PhysRevLett.97.255901.
[46] R.A. Huggins, Simple method to determine electronic and ionic components of the conductivity in mixed conductors A review, Ionics 8 (3–4) (2002) 300–313.
[47] A. Cros, M.O. Aboelfotoh, K.N. Tu, FORMATION, oxidation, electronic, and electrical-properties OF copper silicides, J. Appl. Phys. 67 (7) (1990) 3328–3336, https://doi.org/10.1063/1.345369.
[48] M. Cakar, C. Temirci, A. Turut, The Schottky barrier height of the rectifying Cu/pyronline-B/p-Si, Au/pyronine-B/p-Si, Sn/pyronine-B/p-Si and Al/pyronine-B/p-Si contacts, Synth. Met. 142 (1–3) (2004) 177–180, https://doi.org/10.1016/j.synthmet.2003.08.009.